ADVANCED MATERIALS
www.advmat.de

Inverse Design Strategies for 3D Surfaces Formed by Mechanically Guided Assembly

Zhichao Fan, Yiyuan Yang, Fan Zhang, Zheng Xu, Hangbo Zhao, Taoyi Wang, Honglie Song, Yonggang Huang, John A. Rogers,* and Yihui Zhang**

Deterministic transformations of 2D patterns of materials into well-controlled 3D mesostructures serve as the basis for manufacturing methods that can bypass limitations of conventional 3D micro/nanofabrication. Here, guided mechanical buckling processes provide access to a rich range of complex 3D mesostructures in high-performance materials, from inorganic and organic semiconductors, metals and dielectrics, to ceramics and even 2D materials (e.g., graphene, MoS_2). Previous studies demonstrate that iterative computational procedures can define design parameters for certain targeted 3D configurations, but without the ability to address complex shapes. A technical need is in efficient, generalized inverse design algorithms that directly yield sets of optimized parameters. Here, such schemes are introduced, where the distributions of thicknesses across arrays of separated or interconnected ribbons provide scalable routes to 3D surfaces with a broad range of targeted shapes. Specifically, discretizing desired shapes into 2D ribbon components allows for analytic solutions to the inverse design of centrally symmetric and even general surfaces, in an approximate manner. Combined theoretical, numerical, and experimental studies of ≈20 different 3D structures with characteristic sizes (e.g., ribbon width) ranging from ≈200 µm to ≈2 cm and with geometries that resemble hemispheres, fire balloons, flowers, concave lenses, saddle surfaces, waterdrops, and rodents, illustrate the essential ideas.

Strategies for manufacturing 3D mesostructures in advanced materials are of increasing interest,[1–16] motivated by applications in areas ranging from microelectromechanical and nanoelectromechanical systems (MEMS and NEMS),[17–23] energy storage devices,[24–28] to metamaterials,[7,29–34] to electronic and optoelectronic systems,[35–42] and to biomedical tools.[43–49] Many different manufacturing approaches are now available, including those based on rolling/folding,[50–54] nonplanar bending,[55–57] 3D printing,[58–62] and geometric transformation guided by buckling.[63–69] These latter approaches are particularly attractive due to their compatibility with well-established planar fabrication technologies and advanced thin film materials, as demonstrated through many examples of electronic devices and microelectromechanical systems with unusual and/or enhanced performance due to their 3D

Dr. Z. Fan, Dr. F. Zhang, Z. Xu, Dr. H. Song, Prof. Y. Zhang
Applied Mechanics Laboratory
Department of Engineering Mechanics
Center for Flexible Electronics Technology
Tsinghua University
Beijing 100084, P. R. China
E-mail: yihuizhang@tsinghua.edu.cn

Y. Yang
Departments of Mechanical Engineering
Northwestern University
Evanston, IL 60208, USA

Z. Xu
The State Key Laboratory for Manufacturing and Systems Engineering
School of Mechanical Engineering
Xi'an Jiaotong University
Xi'an 710049, P. R. China

Prof. H. Zhao[+]
Center for Bio-Integrated Electronics
Northwestern University
Evanston, IL 60208, USA

The ORCID identification number(s) for the author(s) of this article can be found under https://doi.org/10.1002/adma.201908424.

[+]Present address: Department of Aerospace and Mechanical Engineering, University of Southern California, Los Angeles, CA 90089, USA

DOI: 10.1002/adma.201908424

T. Wang
Department of Physics
Tsinghua University
Beijing 100084, P. R. China

Prof. Y. Huang
Departments of Civil and Environmental Engineering
Mechanical Engineering, and Materials Science and Engineering
Center for Bio-Integrated Electronics
Northwestern University
Evanston, IL 60208, USA
E-mail: y-huang@northwestern.edu

Prof. J. A. Rogers
Department of Materials Science and Engineering
Biomedical Engineering
Neurological Surgery
Chemistry
Mechanical Engineering
Electrical Engineering and Computer Science
Simpson Querrey Institute and Feinberg Medical School
Center for Bio-Integrated Electronics
Northwestern University
Evanston, IL 60208, USA
E-mail: jrogers@northwestern.edu

architectures.[70–76] A rich diversity of accessible 3D topologies is possible[63–68] as a result of complex mechanical deformations of patterned thin films or multilayers in a transformation process that combines compression/shearing loading at multiple locations across a 2D precursor. Here, the first step is in fabrication of such a precursor structure, followed by transfer printing onto a prestretched elastomeric substrate, where covalent bonding occurs only at precisely selected regions. Release of the prestretch imparts compressive forces at these bonding sites to trigger buckling processes that induce a transformation into a 3D configuration. Key control parameters include the geometry of the 2D precursor structure, the location of the bonding sites and the pre-strain of the substrate.[63–65,69]

Development of an inverse design method to define these parameters for a desired 3D structure could increase the utility of this overall approach. Some techniques have been established for the other types of assembly methods, including flat sheets with prescribed origami and kirigami patterns,[77,78] liquid crystal elastomer sheets with designed nematic director fields,[79,80] pneumatic shape-morphing elastomer with a specific network of airways embedded inside the elastomer.[81] However, these techniques are generally not applicable to the design of buckling-guided 3D assembly, due to fundamental differences in basic operational principles. Previous reports on buckling-guided 3D assembly focus on the analyses of "forward problem" that mainly deals with the prediction of the geometric configuration of assembled 3D mesostructures for a prescribed 2D precursor and loading parameters, either through theoretical modeling[82–95] or numerical simulations.[66,96,97] However, these methods are not applicable or efficient in solving the "inverse problem" that maps the target 3D geometry onto an unknown 2D precursor and loading parameters, because the former applies to limited classes of ribbon geometries, while the latter usually exploits the trial-and-error method and demands an unrealistic number of iterative calculations to determine the design parameters. Although optimization-based approaches[98,99] to inverse design have some utility, they cannot address requirements in 3D surfaces/membranes with complex contours.

This paper introduces a versatile inverse design method that exploits spatial distributions of thickness in 2D precursors as key design parameters, to enable precise reproduction of desired 3D surfaces. To introduce the approach, we begin with simple examples associated with 3D curved ribbons realized by out-of-plane bending, where analytic solutions define the required variations of thickness along the length direction and the pre-strain in the substrate. By incorporating the ribbon width as an additional design parameter, this inverse design method can be extended to reproduce centrally symmetric 3D surfaces in a discretized manner. Using concepts inspired by computed tomography (CT), the same approaches can be utilized to realize surfaces with general shapes. Experimental demonstrations include qualitative and quantitative comparisons between desired and realized 3D geometries, for ≈20 different examples, with feature sizes (e.g., ribbon width) ranging from ≈200 μm to ≈2 cm. A diversity of complex 3D configurations (e.g., those in hemisphere, donut, fire balloon, flower, concave lens, saddle, waterdrop, and rodent shapes) suggest potential applications in functional devices.

Figure 1a provides a schematic illustration of the processes for assembling 3D mesostructures from photolithographically defined 2D precursors (see the Experimental Section for details). Here, greyscale photolithography patterns the thickness and the 2D geometry of a layer of photoresist (AZ 4620), through spatial control of exposure dose. Reactive ion etching transfers this pattern of photoresist into a corresponding structure in an underlying layer of parylene. Here, an oxygen plasma with carefully adjusted pressure and power allows for matching of the rates of etching through the photoresist and the parylene. Release of the resulting pattern of parylene onto a water-soluble tape followed by patterned deposition of SiO_2 through a shadow mask defines a pattern of bonding sites that form upon contact with a pre-stretched silicone elastomer (Dragon Skin; Smooth-On, Easton, PA). Compressive buckling follows from release of the pre-strain, to form a 3D shape. Demonstrations in macroscale structures use printing techniques (Object 260VS, Stratasys) instead of photolithography to create the 2D precursors, and where the bonding sites rely on patterned thin film adhesives.

An analytic model for inverse design applies to the simplest classes of 3D structures realized by buckling of 2D ribbons. Here, the target structure forms through compressive buckling of a straight ribbon with well-defined variation of thickness along its length. Consider a target structure whose axial shape can be characterized by the coordinates $X(S)$ and $Z(S)$ (see Figure 1b and Figure S1, Supporting Information). The curvature (K) of the axis is given by

$$K(S)=\frac{\mathrm{d}^2X(S)}{\mathrm{d}S^2}\frac{\mathrm{d}Z(S)}{\mathrm{d}S}-\frac{\mathrm{d}^2Z(S)}{\mathrm{d}S^2}\frac{\mathrm{d}X(S)}{\mathrm{d}S}, S\in[0,L_\mathrm{s}] \tag{1}$$

where S is the arc length coordinate and L_S is the ribbon length. When $K(S)$ is positive everywhere along the coordinate S, a mechanics model based on the analyses of static equilibrium and Euler–Bernoulli beam theory (see Note S1.1, Supporting Information for details) determines the primary inverse design parameters (i.e., the thickness distribution $t(S)$ and the pre-strain of substrate ε_pre) analytically as

$$t(S)=\frac{t_\mathrm{max}\left[\dfrac{Z(S)}{E(S)w(S)K(S)}\right]^{\frac{1}{3}}}{\max\left[\dfrac{Z(S)}{E(S)w(S)K(S)}\right]^{\frac{1}{3}}} \tag{2}$$

$$\varepsilon_\mathrm{pre}=\frac{L_\mathrm{S}-[X(L_\mathrm{S})-X(0)]}{[X(L_\mathrm{S})-X(0)]+L_\mathrm{bonding}} \tag{3}$$

where $E(S)$ is the Young's modulus, $w(S)$ is the width, t_max is the maximum value of thickness along the entire length of the ribbon, and L_bonding is the length of bonding site (see Note S1.1, Supporting Information for details). The top four structures (marked by "A," "B," "E," and "F") of Figure 1b belong to this type of geometry (i.e., with positive $K(S)$ everywhere). The axial coordinates of the target configurations and the corresponding inverse design solutions of these structures are in Note S1.3

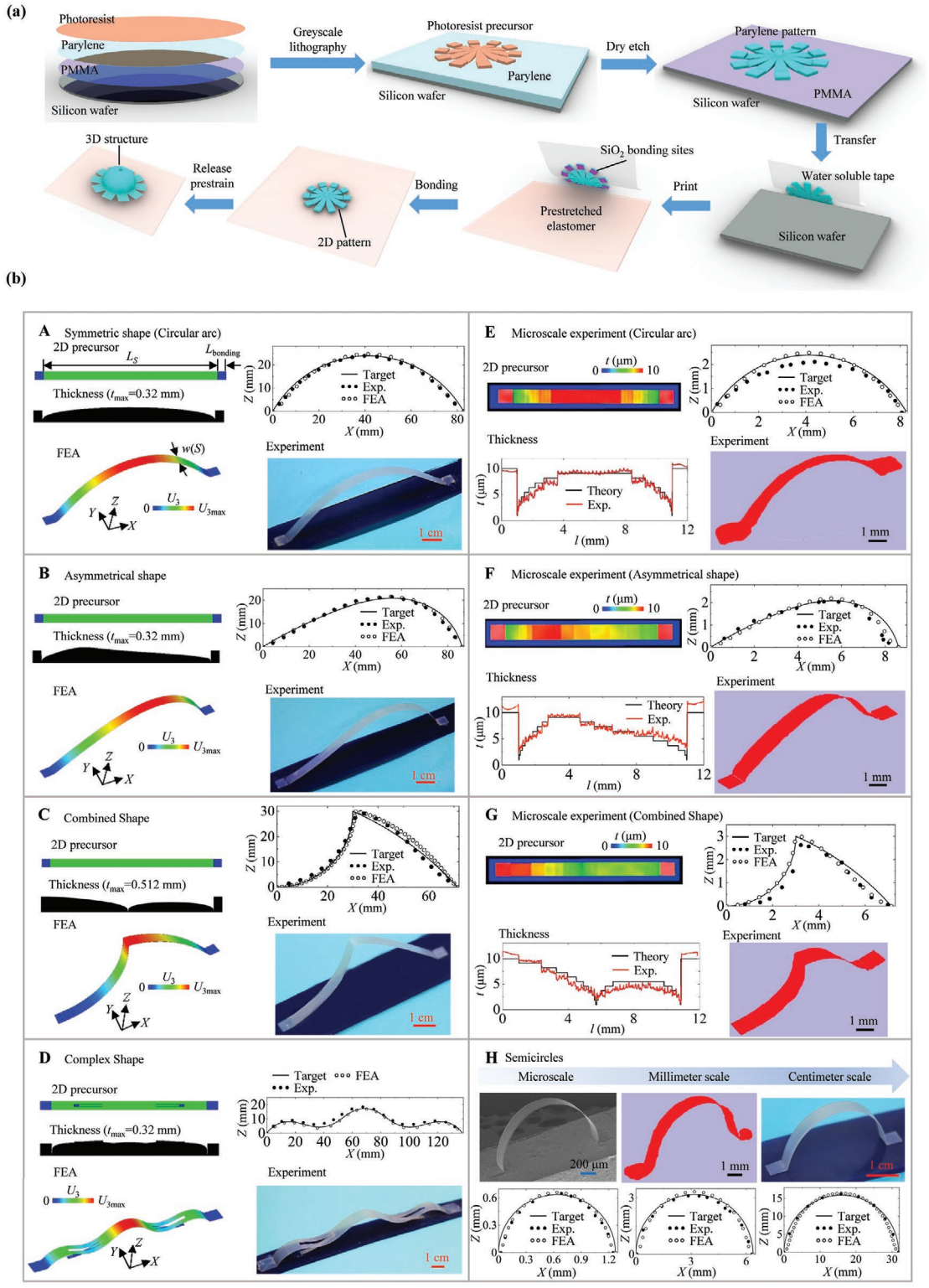

Figure 1. Conceptual illustration of the fabrication approach and representative results of inverse design of a variety of 3D curved ribbon structures. a) Schematic illustration of the process for fabricating 3D mesostructures by compressive buckling of 2D precursor structures with spatially varying distributions of thickness. b) Representative results of the inverse design of 3D curved ribbon structures with a range of different length scales. (A)–(G) show 2D precursors designed by theoretical analysis and corresponding 3D structures based on experiments (SEM/optical images) and finite-element analysis (FEA).

(Supporting Information). The Young's modulus $E(S)$ and the width $w(S)$ are constants in all of these cases. The experimental approximations to the thickness distributions $t(S)$ involve: i) regions with zero thickness replaced with small thicknesses (e.g., $t_{max}/10$); ii) continuous distributions discretized as 10 different thickness values (for the photolithographically defined precursors) and more than 20 values (for the printed precursors). The thicknesses at the bonding sites are set to t_{max}, without loss of generality. The thickness distributions (left top panel in Figure 1b, A and B) defined by this inverse design method yield 3D structures that agree remarkably well with the target shapes. For the case of microscale structures, slight differences follow from nonideal thickness variations due to limitations in grayscale photolithography and etching, as shown in Figure 1b (E and F).

When $K(S)$ is not positive everywhere across the target shape, the inverse design method must incorporate additional schemes. Figure 1b (D) presents an example with a complex distribution of curvature in the target shape, changing its sign four times between positive and negative. In this case, the addition of assist features imparts concentrated forces (along the out-of-plane direction, i.e., Z-axis direction) at desired locations, such that the necessary static equilibrium conditions can be satisfied in the target structure (see Note S1.1 and Figure S2, Supporting Information for details). Here, two inner ribbons in the 2D precursor structure connect directly to the substrate. The locations and geometrical parameters of these ribbons can be obtained theoretically from mechanics analysis (see Note S1.1, Supporting Information for details). Figure 1b (D) shows that the resulting structure is in reasonable agreement with the target configuration. Figure 1b (C and G) presents an example that contains a discontinuity point (in terms of the slope) in the target shape. In this case, a crease at this point allows the ribbon to be divided into two segments in the analyses, such that the thickness distributions for each segment can be determined analytically (see Note S1.2 and Figure S3, Supporting Information for details). As shown in Figure 1b (C and G), the target shape can be reproduced in experiments at the macro and millimeter scales. Figure 1b (H) provides an example with a semicircle ribbon configuration, with 3D structures that have three different length scales (with the ribbon width from ≈200 μm to ≈0.5 cm).

Figure 2 illustrates an extension of this method to centrally symmetric 3D surfaces. Such 3D surfaces are mostly nondevelopable, and thereby, cannot be realized directly by buckling of 2D structures at small material strains. Here, an approximate inverse design method relies on the concept of discretization, where the target 3D surface is divided evenly into (n) segments (Figure 2a). Each segment can be regarded as a 2D curved ribbon with varying width, and the shape of the ribbon axis is the same as the generatrix of the surface. The accuracy of such an approximation increases with the number n (Figure 2a), through a quantitative relationship given in Note S2.1 (Supporting Information). In the current study, n is 10, as shown by the results in Figure 2 and **Figure 3**. To keep the ribbon components connected with each other during the 3D assembly, the ending points of the radial cuts have a distance of (aL_S) from the center of the 2D precursor. Based on the geometry of the target 3D shape, the width distribution of each ribbon segment in the 2D precursor can be determined accurately as

$$w(S) = \frac{2\pi|X(S)|}{n},\ S \in \left[0, \frac{L_S}{2} - aL_S\right] \cap \left[\frac{L_S}{2} + aL_S, L_S\right] \tag{4}$$

where $|X(S)|$ is the absolute coordinate value of the ribbon cross section, namely, the distance between the specified cross section and the center of the entire 2D precursor. Consistent with the previous analyses, when the curvature $K(S)$ of the generatrix of the target 3D surface is positive everywhere, the thickness distribution can be determined by Equation (2), and the thickness of the undivided center part is set as a constant value $t(L_S/2 + aL_S)$ to ensure the continuity of the thickness (see Note S2.1 and Figure S4, Supporting Information for details). To this end, inverse design of centrally symmetric 3D surfaces is equivalent to that of curved ribbons with varying widths, and an analytic solution of the thickness distribution can be obtained.

Figure 2b provides theoretical and experimental results for three centrally symmetric convex surfaces, including a hemisphere (A), drum (B), and fire balloon (C). As the curvature is positive throughout the surface, the target shapes can be reproduced by exploiting appropriate thickness distributions, without the need to introduce additional assist features. The parametric equation of the generatrix and the design parameters of these surfaces are in Note S2.2 (Supporting Information). For the hemisphere-like and drum-like structures in Figure 2b (A and B), a copper layer (150 nm) deposited after the buckling assembly enhances the reflections for improved visibility of the curvature. In all examples, the optical images are in close accordance with the target shapes. Figure 2c presents results of millimeter scale experiments, including measured thickness distributions versus those determined by theoretical analyses, comparisons of generatrix configurations between the target shapes and experiments, as well as SEM images of the resulting mesostructures. The differences for the drum-like mesostructure can be attributed to discrepancies between the experimentally realized thickness distribution and the computed one, especially at the region of large thickness gradient.

Figure 3 illustrates inverse design of four different centrally symmetric surfaces that contain concave regions. In the top two structures (A and B), the curvature of the generatrix is not positive everywhere, and in this case, additional assist features apply forces to specified locations (see Note S2.2, Supporting Information for details), similar to the strategy described previously. In the bottom two structures that resemble a flower (C) and a concave lens (D), a small central part of the target shape is approximately flat. Here, we incorporate a bonding region at the corresponding location of the 2D precursor structure. For the flower-like structure, the generatrix is approximated by a circular arc. Consequently, the width distribution of the ribbon segment to serve as the flower petal can be obtained from Equation (4). The outer ribbon segment that assists the formation of the inner segment has a constant width for simplicity, and its thickness distribution can be obtained according to Equation (2). For the structure that resembles a concave lens (D), the generatrix contains a point with a discontinuity of the slope. In this case, the computed thickness distribution is similar to that of the combined ribbon structure in

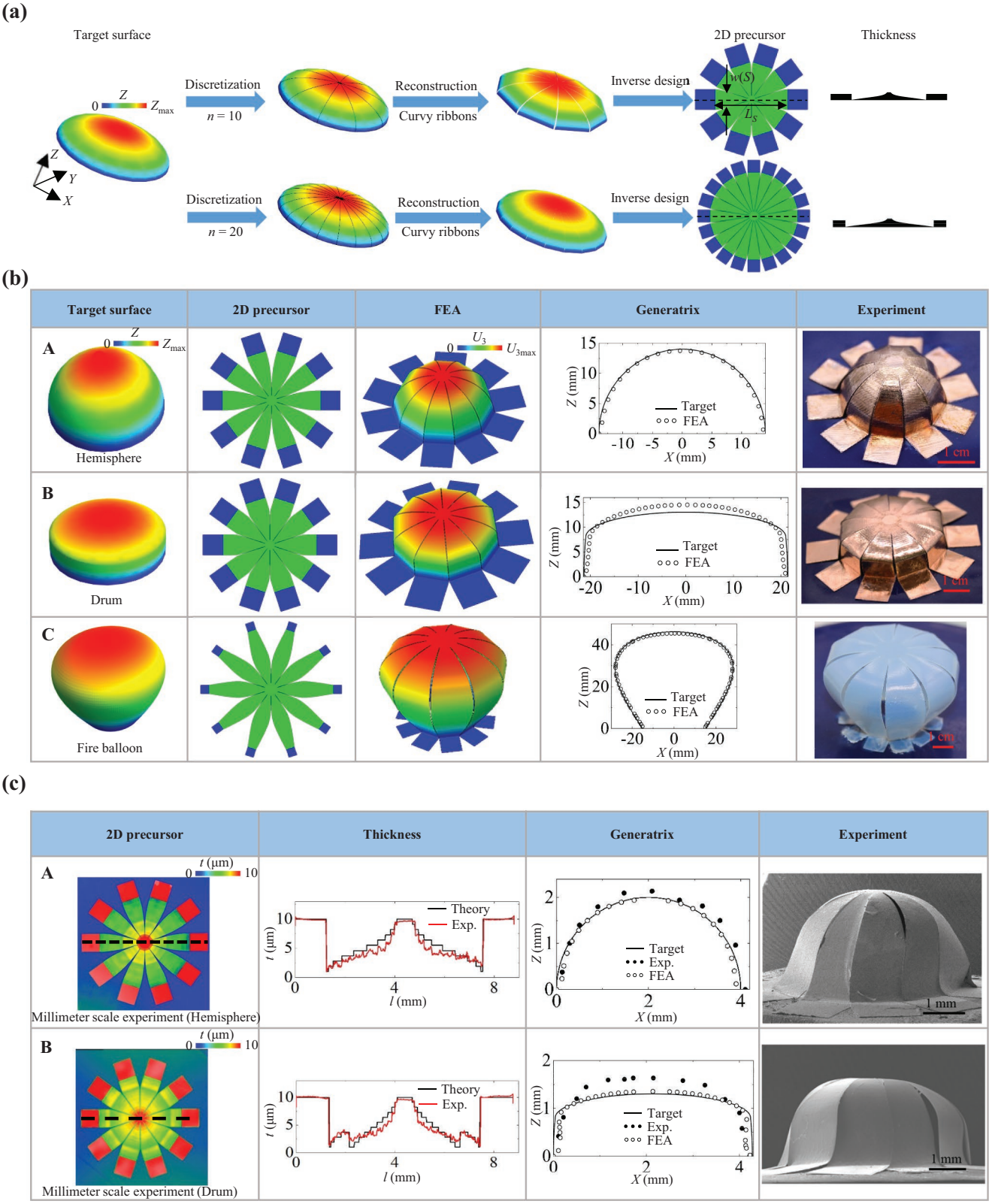

Figure 2. Inverse design for centrally symmetric surfaces with convex configurations. a) Schematic illustration of the discretized design approach for centrally symmetric surfaces. b) Results of inverse design for hemisphere (A), drum (B), and fire balloon (C) shapes, including 2D precursors designed by theoretical analyses and corresponding 3D structures based on centimeter-scale experiments and FEA. c) Similar results for the hemisphere (A) and drum (B) in parylene, based on millimeter-scale experiments.

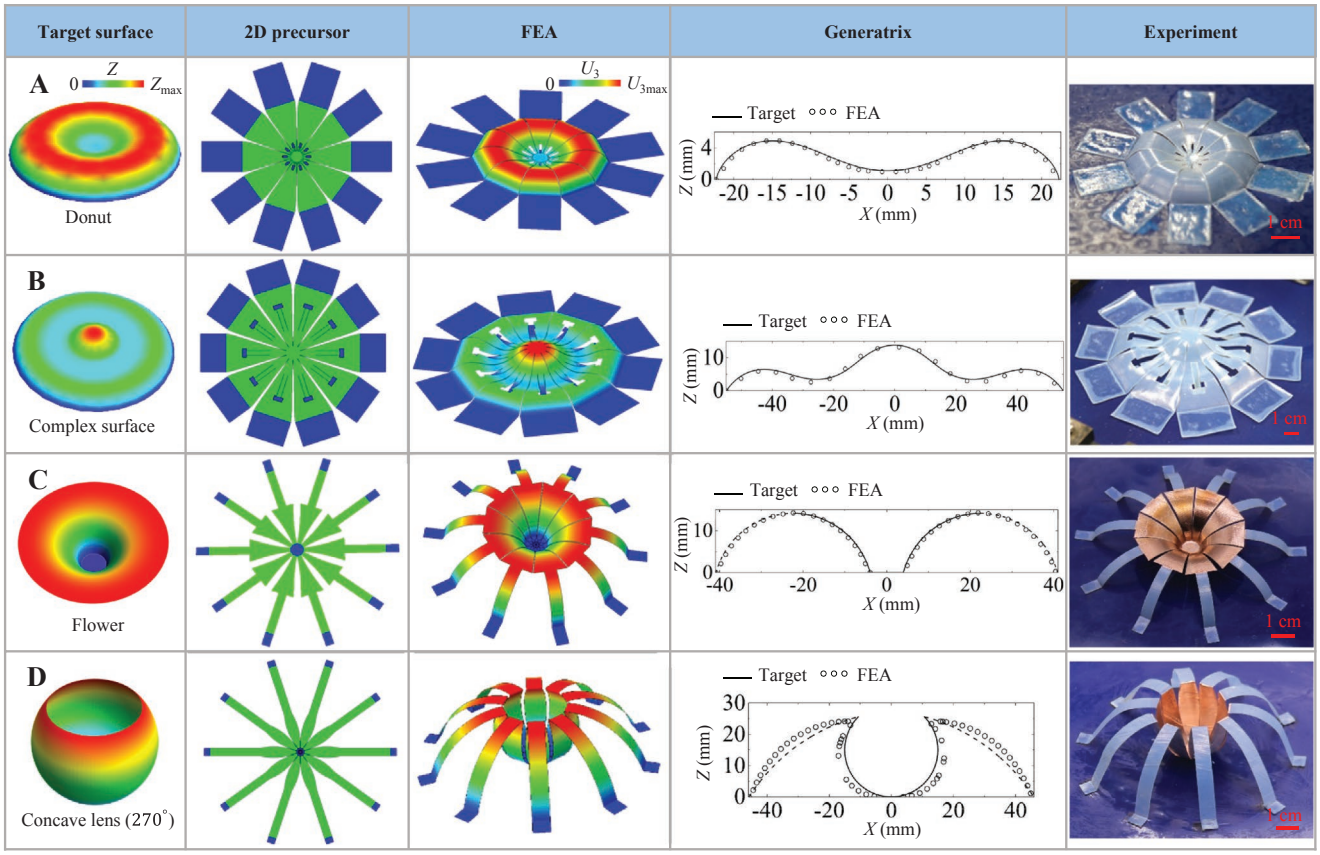

Figure 3. Inverse design for centrally symmetric surfaces that contain concave configurations. A–D) Results for donut (A), complex surface (B), flower (C), and concave lens (270°) (D) shapes, including the 2D precursors designed by theoretical analyses and corresponding 3D structures based on centimeter-scale experiments and FEA.

Figure 1b (C and G). In all of the above examples, the configurations of assembled 3D structures agree reasonably well with the target shapes. Figure S5 (Supporting Information) provides three additional examples.

Figure 4 introduces concepts inspired by CT, as routes to general, nondevelopable 3D surfaces without any central symmetry. With a saddle surface as an example, Figure 4a illustrates the general strategy. The CT-scan method (scan direction along the *Y* axis) yields profile information (*n* segments) for the target surface, to define a set of ribbons with profiles and widths to reconstruct the surface. Inverse design on a per ribbon basis yields the target 3D surface in an approximate manner. According to Equation (3) and the different target profiles of the ribbon components, the lengths of bonding sites for each component can be derived as

$$L_{\text{bonding}(i)} = \frac{L_{S(i)} - (1+\varepsilon_{\text{pre}})\left[X_{(i)}\left(L_{S(i)}\right) - X_{(i)}(0)\right]}{\varepsilon_{\text{pre}}}, i = 1,2,3,\cdots n \quad (5)$$

where the subscript (i) denotes the ribbon index. Typically, a proper value of the pre-strain ε_{pre} should be selected, such that the bonding lengths of all ribbon components are in a feasible range. Considering that the bonding length should also be sufficiently large (e.g., comparable to or larger than the ribbon width, according to previously reported experiments) to avoid the delamination of bonding sites, a practicable criterion can be written as

$$\text{Min}\left(L_{\text{bonding}(i)}\right) = w \quad (6)$$

where w is the ribbon width determined by the space of the CT scan. Equation (6) requires that the length of the shortest bonding site is the same as the ribbon width. Inverse design of each ribbon component can then be completed using the aforementioned methods (see Note S3.1 and Figure S6, Supporting Information for details).

Figure 4b presents the results for a saddle surface (A) and a "waterdrop" (B). Since the curvatures are all positive, the inverse design parameters can be obtained from Equations (2), (3), and (5). Here, 15 and 14 ribbon components reconstruct the saddle and the waterdrop, respectively, for reasonably good agreement with the target surfaces. Expressions for the target surfaces and the ribbon profiles are in Note S3.2 (Supporting Information). Figure 4c demonstrates the inverse design of a surface in the form of a rodent, with the target surface shown in the left middle and bottom panels from two different views. Elliptic curves serve as best fit approximations to the profile curves, to facilitate inverse design of those curved ribbons, owing to the positive curvature of elliptic curves. Since this model has some suspended parts with spatially varying heights, the bonding sites adopt different heights for each ribbon. The 2D

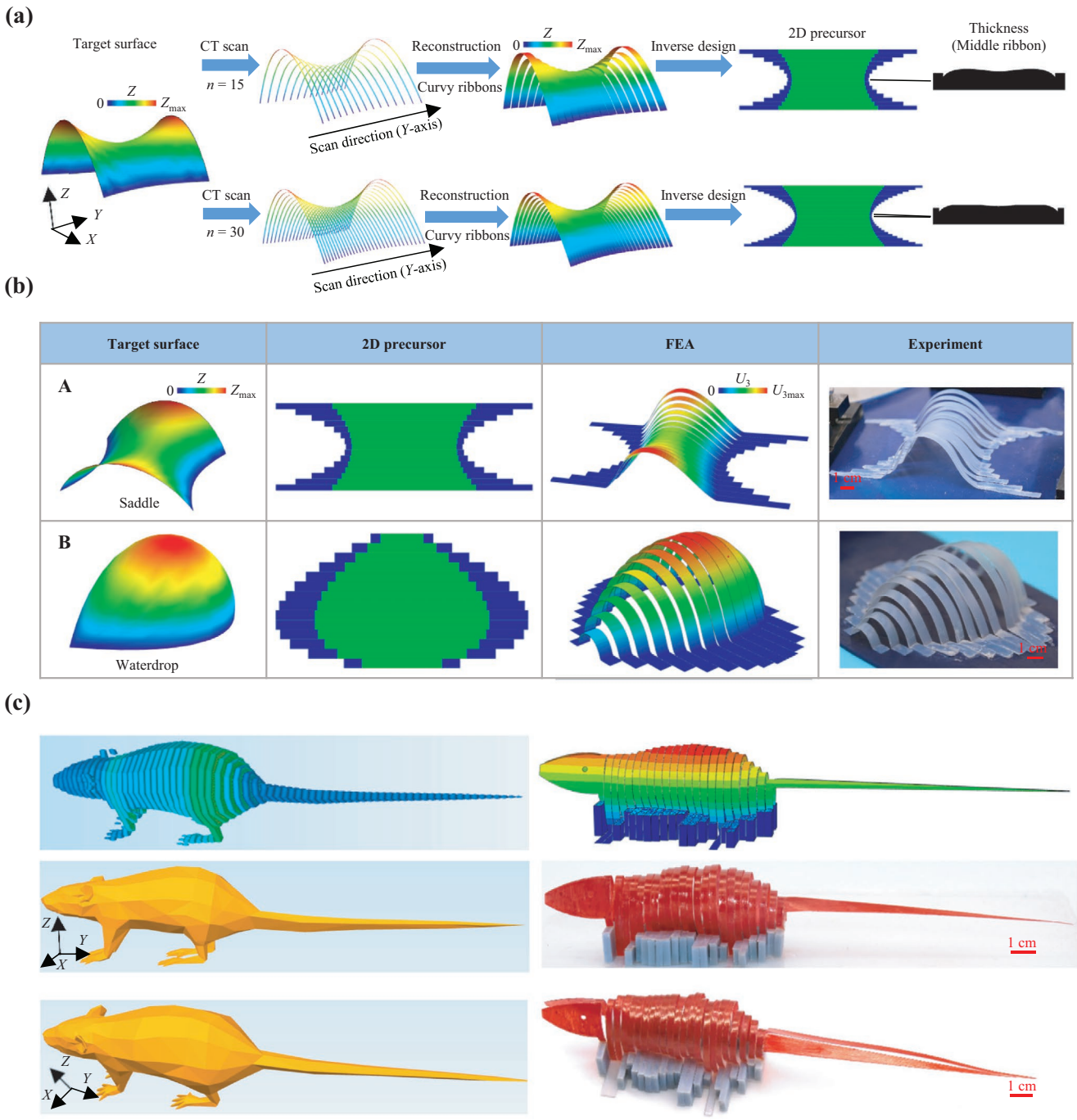

Figure 4. Inverse design for general surfaces without any central symmetry. a) Schematic illustration of the discretized design approach for general surfaces. b) Results of inverse design for saddle (A) and waterdrop (B) shapes, including the 2D precursors and corresponding 3D structures based on centimeter-scale experiments and FEA. c) Similar results for a rodent model.

precursor and the height distribution of the bonding sites are in Figure S7 (Supporting Information). Since the head and tail of the rodent are much smaller than the body, patterned membranes serve as the basis to reconstruct these two regions. The FEA and optical images of the assembled structure look quite similar to the target shape. An additional example in the form of a cartoon face appears in Figure S8 and Note S4 (Supporting Information), with two spherical and a conical surface.

In conclusion, we introduce an analytic inverse design method for designing 3D ribbon shapes through use of the spatially varying thicknesses and assist features in corresponding 2D precursors. By discretizing target 3D surfaces into a set of ribbon components, this analytic development allows for inverse design of centrally-symmetric surfaces and more general surfaces in an approximate manner. Demonstrations across a variety of complex 3D configurations (e.g., fire

balloon, donut, flower, concave lens, saddle surface, waterdrop, and rodent) suggest general applicability of these methods. The ideas allow for rational assembly of 3D mesostructures with surface geometries precisely matched to target configurations, of possible utility in devices that demand accurately tailored 3D geometries, such as antennas, high-precision sensors and bio-integrated electronic systems.

Experimental Section

Assembly of 3D Structures: A silicon wafer served as the substrate. Spin coating poly(methyl methacrylate) (PMMA A8; 3000 rpm, 30 s) formed a sacrificial layer for transfer printing. Chemical vapor deposition (SCS Labcoater 2, PDS 2010) yielded a uniform film of parylene (15 μm) on the PMMA. Here, a slightly thicker parylene (as compared to the maximum thickness (10 μm) required for the final 2D precursor) can facilitate the subsequent fabrication processes, noting that the excess is removed by reactive ion etching (RIE). Spin casting (1000 rpm, 30 s) and soft baking (110 °C, 3 min) defined a film of photoresist (AZ 4620; 10 μm) on the parylene. Grey lithographic patterning (Heidelberg MLA 150; maximum dose: 500 mJ; wavelength: 375 nm; develop: 100 s in AZ 400K developer diluted with water in a 1:2 volume ratio) of the photoresist defined structures with desired patterns and thickness distributions. Reactive ion etching (SAMCO Inc) with an oxygen plasma (Pressure: 26.7 Pa, Power: 100 W, O_2: 100 SCCM) transferred the pattern of photoresist into a corresponding pattern in the parylene. A 3D optical profiler (Zygo) quantified the geometric features of these parylene precursors. Dissolving the PMMA in acetone allowed retrieval of the precursor onto the surface of a water-soluble tape (AQUASOL). A film of polyimide (75 μm) patterned by laser ablation served as a shadow mask for electron beam deposition of Ti (15 nm)/ SiO_2 (100 nm) to define bonding sites on the precursor. Exposing a pre-stretched silicone elastomer (Dragon Skin 10 Slow) and the precursor to ultraviolet induced ozone created surface hydroxyl termination. Laminating the precursor on the elastomer, followed by baking in a 70 °C convection oven for 10 min, created strong adhesion at the bonding sites. Finally, dissolving the water soluble tape in warm water and releasing the pre-strain completed the assembly of the 3D structures.

Macroscale 3D structures used 2D precursors defined by a 3D printer (Object 260VS, Stratasys) in Veroblue, transferred onto a prestretched silicone substrate (≈3 mm in thickness, Dragon Skin, Smooth-On) with strong covalent bonding produced by a commercial adhesive (Super Glue, Gorilla Glue Company). Release of the pre-stretch triggered the 2D-to-3D transformation, thereby completing the 3D assembly.

Finite Element Analysis (FEA): Four-node shell elements (S4R in commercial software ABAQUS) were adopted for the 2D precursors. Refined meshes were used to ensure the computational accuracy. The elastic modulus (E) and Poisson's ratio (υ) are $E_{Veroblue}$ = 2 GPa and $\upsilon_{Veroblue}$ = 0.3 for Veroblue used in macroscale experiments, and $E_{Parylene}$ = 2.7 GPa and $\upsilon_{Parylene}$ = 0.4 for Parylene used in microscale experiments. Geometrical imperfections obtained from the linear-buckling analyses were employed in the simulations of the postbuckling processes that yielded the predicted 3D configurations of buckling-guided assembly.

Supporting Information

Supporting Information is available from the Wiley Online Library or from the author.

Acknowledgements

Z.F. and Y.Y. contributed equally to this work. Y.Z. acknowledges the support from the National Natural Science Foundation of China (Grant Nos. 11672152, 11722217, and 11921002), the Tsinghua University Initiative Scientific Research Program (# 2019Z08QCX10), and the Tsinghua National Laboratory for Information Science and Technology. J.A.R. acknowledges the support from Soft and Hybrid Nanotechnology Experimental (SHyNE) Resource (NSF ECCS-1542205), the Materials Research Science and Engineering Center (DMR-1720139), the State of Illinois, and Northwestern University. Y.H. acknowledges the support from the NSF (Grant No. CMMI1635443). Z.F. acknowledges support from the National Natural Science Foundation of China (Grant No. 11802154).

Conflict of Interest

The authors declare no conflict of interest.

Keywords

3D assembly, 3D mesostructures, analytic modeling, inverse design

Received: December 24, 2019
Revised: January 29, 2020
Published online: February 25, 2020

[1] S. Babaee, J. Shim, J. C. Weaver, E. R. Chen, N. Patel, K. Bertoldi, *Adv. Mater.* **2013**, *25*, 5044.
[2] C. J. Wang, K. Sim, J. Chen, H. Kim, Z. Y. Rao, Y. H. Li, W. Q. Chen, J. Z. Song, R. Verduzco, C. J. Yu, *Adv. Mater.* **2018**, *30*, 1706695.
[3] C. Yu, Z. Duan, P. Yuan, Y. Li, Y. Su, X. Zhang, Y. Pan, L. L. Dai, R. G. Nuzzo, Y. Huang, *Adv. Mater.* **2013**, *25*, 1541.
[4] H. Gao, R. Tang, T. Ma, H. Q. Jiang, H. Y. Yu, G. J. Cheng, *J. Microelectromech. Syst.* **2015**, *24*, 414.
[5] D. Jang, L. R. Meza, F. Greer, J. R. Greer, *Nat. Mater.* **2013**, *12*, 893.
[6] E. T. Filipov, G. Paulino, T. Tachi, *Proc. R. Soc. A* **2016**, *472*, 20150607.
[7] E. T. Filipov, T. Tachi, G. H. Paulino, *Proc. Natl. Acad. Sci. USA* **2015**, *112*, 12321.
[8] L. R. Meza, A. J. Zelhofer, N. Clarke, A. J. Mateos, D. M. Kochmann, J. R. Greer, *Proc. Natl. Acad. Sci. USA* **2015**, *112*, 11502.
[9] L. R. Meza, S. Das, J. R. Greer, *Science* **2014**, *345*, 1322.
[10] J. Huang, J. Liu, B. Kroll, K. Bertoldi, D. R. Clarke, *Soft Matter* **2012**, *8*, 6291.
[11] A. H. Rahmati, S. Y. Yang, S. Bauer, P. Sharma, *Soft Matter* **2019**, *15*, 127.
[12] Z. Liu, D. Qi, W. R. Leow, J. Yu, M. Xiloyannnis, L. Cappello, Y. Liu, B. Zhu, Y. Jiang, G. Chen, L. Masia, B. Liedberg, X. Chen, *Adv. Mater.* **2018**, *30*, 1707285.
[13] S. Yin, Z. Niu, X. Chen, *Small* **2012**, *8*, 2458.
[14] Q. Liu, B. Xu, *Soft Matter* **2018**, *14*, 5968.
[15] X. Cheng, Y. Zhang, *Adv. Mater.* **2019**, *31*, 1901895.
[16] W. Pang, X. Cheng, H. Zhao, X. Guo, Z. Ji, G. Li, Y. Liang, Z. Xue, H. Song, F. Zhang, Z. Xu, L. Sang, W. Huang, T. Li, Y. Zhang, *Natl. Sci. Rev.* **2019**, nwz164.
[17] R. J. Wood, *Am. Sci.* **2014**, *102*, 124.
[18] D. Bishop, F. Pardo, C. Bolle, R. Giles, V. Aksyuk, *J. Low Temp. Phys.* **2012**, *169*, 386.
[19] J. Rogers, Y. G. Huang, O. G. Schmidt, D. H. Gracias, *MRS Bull.* **2016**, *41*, 123.
[20] R. Songmuang, A. Rastelli, S. Mendach, O. G. Schmidt, *Appl. Phys. Lett.* **2007**, *90*, 091905.
[21] O. G. Schmidt, K. Eberl, *Nature* **2001**, *410*, 168.
[22] Y. Chen, B. Xu, Y. Mei, *Chem. - Asian J.* **2019**, *14*, 2472.

[23] G. Huang, Y. Mei, *Small* **2018**, *14*, 1703665.
[24] X. C. Xiao, W. D. Zhou, Y. N. Kim, I. Ryu, M. Gu, C. M. Wang, G. Liu, Z. Y. Liu, H. J. Gao, *Adv. Funct. Mater.* **2015**, *25*, 1426.
[25] L. Ye, M. Liao, H. Sun, Y. Yang, C. Tang, Y. Zhao, L. Wang, Y. Xu, L. Zhang, B. Wang, F. Xu, X. Sun, Y. Zhang, H. Dai, P. G. Bruce, H. Peng, *Angew. Chem., Int. Ed.* **2019**, *58*, 2437.
[26] C. Zhu, T. Y. Liu, F. Qian, W. Chen, S. Chandrasekaran, B. Yao, Y. Song, E. B. Duoss, J. D. Kuntz, C. M. Spadaccini, M. A. Worsley, Y. Li, *Nano Today* **2017**, *15*, 107.
[27] Z. M. Song, T. Ma, R. Tang, Q. Cheng, X. Wang, D. Krishnaraju, R. Panat, C. K. Chan, H. Y. Yu, H. Q. Jiang, *Nat. Commun.* **2014**, *5*, 3140.
[28] H. L. Ning, J. H. Pikul, R. Y. Zhang, X. J. Li, S. Xu, J. J. Wang, J. A. Rogers, W. P. King, P. V. Braun, *Proc. Natl. Acad. Sci. USA* **2015**, *112*, 6573.
[29] W. N. Xu, K. S. Kwok, D. H. Gracias, *Acc. Chem. Res.* **2018**, *51*, 436.
[30] J. Valentine, S. Zhang, T. Zentgraf, E. Ulin-Avila, D. A. Genov, G. Bartal, X. Zhang, *Nature* **2008**, *455*, 376.
[31] D. Chanda, K. Shigeta, S. Gupta, T. Cain, A. Carlson, A. Mihi, A. J. Baca, G. R. Bogart, P. Braun, J. A. Rogers, *Nat. Nanotechnol.* **2011**, *6*, 402.
[32] J. K. Gansel, M. Thiel, M. S. Rill, M. Decker, K. Bade, V. Saile, G. von Freymann, S. Linden, M. Wegener, *Science* **2009**, *325*, 1513.
[33] Y. Tang, G. Lin, S. Yang, Y. K. Yi, R. D. Kamien, J. Yin, *Adv. Mater.* **2016**, *29*, 1604262.
[34] D. M. Sussman, Y. Cho, T. Castle, X. T. Gong, E. Jung, S. Yang, R. D. Kamien, *Proc. Natl. Acad. Sci. USA* **2015**, *112*, 7449.
[35] J. H. Lee, C. Y. Koh, J. P. Singer, S. J. Jeon, M. Maldovan, O. Stein, E. L. Thomas, *Adv. Mater.* **2014**, *26*, 532.
[36] Y. H. Li, J. P. Zhang, Y. F. Xing, J. Z. Song, *AIP Adv.* **2018**, *8*, 055102.
[37] Y. Cui, Y. H. Li, Y. F. Xing, T. Z. Yang, J. Z. Song, *Int. J. Therm. Sci.* **2018**, *127*, 321.
[38] M. Schumann, T. Buckmann, N. Gruhler, M. Wegener, W. Pernice, *Light: Sci. Appl.* **2014**, *3*, 175.
[39] C. Choi, M. K. Choi, S. Liu, M. S. Kim, O. K. Park, C. Im, J. Kim, X. Qin, G. J. Lee, K. W. Cho, M. Kim, E. Joh, J. Lee, D. Son, S.-H. Kwon, N. L. Jeon, Y. M. Song, N. Lu, D.-H. Kim, *Nat. Commun.* **2017**, *8*, 1664.
[40] M. Boncheva, S. A. Andreev, L. Mahadevan, A. Winkleman, D. R. Reichman, M. G. Prentiss, S. Whitesides, G. M. Whitesides, *Proc. Natl. Acad. Sci. USA* **2005**, *102*, 3924.
[41] F. Xu, W. Lu, Y. Zhu, *ACS Nano* **2011**, *5*, 672.
[42] K. Sim, S. Chen, Z. Li, Z. Rao, J. Liu, Y. Lu, S. Jang, F. Ershad, J. Chen, J. Xiao, *Nat. Electron.* **2019**, *2*, 471.
[43] S. S. Yao, P. Swetha, Y. Zhu, *Adv. Healthcare Mater.* **2018**, *7*, 1700889.
[44] R. Feiner, L. Engel, S. Fleischer, M. Malki, I. Gal, A. Shapira, Y. Shacham-Diamand, T. Dvir, *Nat. Mater.* **2016**, *15*, 679.
[45] D.-H. Kim, N. Lu, R. Ghaffari, Y.-S. Kim, S. P. Lee, L. Xu, J. Wu, R.-H. Kim, J. Song, Z. Liu, *Nat. Mater.* **2011**, *10*, 316.
[46] X. C. Dai, W. Zhou, T. Gao, J. Liu, C. M. Lieber, *Nat. Nanotechnol.* **2016**, *11*, 776.
[47] D. D. Karnaushenko, D. Karnaushenko, D. Makarov, O. G. Schmidt, *NPG Asia Mater.* **2015**, *7*, e188.
[48] V. A. Bolaños Quiñones, H. Zhu, A. A. Solovev, Y. Mei, D. H. Gracias, *Adv. Biosyst.* **2018**, *2*, 1870113.
[49] M. Yin, L. Xiao, Q. Liu, S.-Y. Kwon, Y. Zhang, P. R. Sharma, L. Jin, X. Li, B. Xu, *Adv. Healthcare Mater.* **2019**, *8*, 1901170.
[50] K. Kobayashi, C. Yoon, S. H. Oh, J. V. Pagaduan, D. H. Gracias, *ACS Appl. Mater. Interfaces* **2019**, *11*, 151.
[51] Y. Y. Dou, B. S. Wang, M. L. Jin, Y. Yu, G. F. Zhou, L. L. Shui, *J. Micromech. Microeng.* **2017**, *27*, 113002.
[52] N. B. Crane, O. Onen, J. Carballo, Q. Ni, R. Guldiken, *Microfluid. Nanofluid.* **2013**, *14*, 383.
[53] Y. Kim, H. Yuk, R. K. Zhao, S. A. Chester, X. H. Zhao, *Nature* **2018**, *558*, 274.
[54] J. V. I. Timonen, M. Latikka, L. Leibler, R. H. A. Ras, O. Ikkala, *Science* **2013**, *341*, 253.
[55] Y. M. Song, Y. Xie, V. Malyarchuk, J. Xiao, I. Jung, K. J. Choi, Z. Liu, H. Park, C. Lu, R. H. Kim, R. Li, K. B. Crozier, Y. Huang, J. A. Rogers, *Nature* **2013**, *497*, 95.
[56] I. W. Jung, J. L. Xiao, V. Malyarchuk, C. F. Lu, M. Li, Z. J. Liu, J. Yoon, Y. G. Huang, J. A. Rogers, *Proc. Natl. Acad. Sci. USA* **2011**, *108*, 1788.
[57] H. Park, H. Cho, J. Kim, J. W. Bang, S. Seo, Y. Rahmawan, D. Y. Lee, K. Y. Suh, *Small* **2014**, *10*, 52.
[58] L. M. Huang, R. Q. Jiang, J. J. Wu, J. Z. Song, H. Bai, B. G. Li, Q. Zhao, T. Xie, *Adv. Mater.* **2017**, *29*, 1605390.
[59] R. L. Truby, J. A. Lewis, *Nature* **2016**, *540*, 371.
[60] S. V. Murphy, A. Atala, *Nat. Biotechnol.* **2014**, *32*, 773.
[61] S. A. Nauroze, L. S. Novelino, M. M. Tentzeris, G. H. Paulino, *Proc. Natl. Acad. Sci. USA* **2018**, *115*, 13210.
[62] Q. Ge, C. K. Dunn, H. J. Qi, M. L. Dunn, *Smart Mater. Struct.* **2014**, *23*, 094007.
[63] Y. H. Zhang, F. Zhang, Z. Yan, Q. Ma, X. L. Li, Y. G. Huang, J. A. Rogers, *Nat. Rev. Mater.* **2017**, *2*, 1.
[64] Y. H. Zhang, Z. Yan, K. W. Nan, D. Q. Xiao, Y. H. Liu, H. W. Luan, H. R. Fu, X. Z. Wang, Q. L. Yang, J. C. Wang, W. Ren, H. Z. Si, F. Liu, L. H. Yang, H. J. Li, J. T. Wang, X. L. Guo, H. Y. Luo, L. Wang, Y. G. Huang, J. A. Rogers, *Proc. Natl. Acad. Sci. USA* **2015**, *112*, 11757.
[65] S. Xu, Z. Yan, K. I. Jang, W. Huang, H. R. Fu, J. Kim, Z. Wei, M. Flavin, J. McCracken, R. Wang, A. Badea, Y. Liu, D. Q. Xiao, G. Y. Zhou, J. Lee, H. U. Chung, H. Y. Cheng, W. Ren, A. Banks, X. L. Li, U. Paik, R. G. Nuzzo, Y. G. Huang, Y. H. Zhang, J. A. Rogers, *Science* **2015**, *347*, 154.
[66] Z. Yan, F. Zhang, F. Liu, M. D. Han, D. P. Ou, Y. H. Liu, Q. Lin, X. L. Guo, H. R. Fu, Z. Q. Xie, M. Y. Gao, Y. M. Huang, J. Kim, Y. T. Qiu, K. W. Nan, J. Kim, P. Gutruf, H. Y. Luo, A. Zhao, K. C. Hwang, Y. G. Huang, Y. H. Zhang, J. A. Rogers, *Sci. Adv.* **2016**, *2*, 1601014.
[67] Z. Song, C. Lv, M. B. Liang, V. Sanphuang, K. Wu, B. Chen, Z. Zhao, J. Bai, X. Wang, J. L. Volakis, L. P. Wang, X. M. He, Y. Yao, S. Tongay, H. Q. Jiang, *Small* **2016**, *12*, 5401.
[68] H. Fu, K. Nan, W. Bai, W. Huang, K. Bai, L. Lu, C. Zhou, Y. Liu, F. Liu, J. Wang, M. Han, Z. Yan, H. Luan, Y. Zhang, Y. Zhang, J. Zhao, X. Cheng, M. Li, J. W. Lee, Y. Liu, D. Fang, X. Li, Y. Huang, Y. Zhang, J. A. Rogers, *Nat. Mater.* **2018**, *17*, 268.
[69] Z. Yan, F. Zhang, J. Wang, F. Liu, X. Guo, K. Nan, Q. Lin, M. Gao, D. Xiao, Y. Shi, Y. Qiu, H. Luan, J. H. Kim, Y. Wang, H. Luo, M. Han, Y. Huang, Y. Zhang, J. A. Rogers, *Adv. Funct. Mater.* **2016**, *26*, 2629.
[70] F. Liu, Y. Chen, H. Song, F. Zhang, Z. Fan, Y. Liu, X. Feng, J. A. Rogers, Y. Huang, Y. Zhang, *Small* **2019**, *15*, 1804055.
[71] F. Liu, X. Cheng, F. Zhang, Y. Chen, H. Song, Y. Huang, Y. Zhang, *Adv. Electron. Mater.* **2019**, *5*, 1900256.
[72] F. Zhang, F. Liu, Y. Zhang, *Sci. China: Technol. Sci.* **2019**, *62*, 243.
[73] S. M. Won, H. Wang, B. H. Kim, K. Lee, H. Jang, K. Kwon, M. Han, K. E. Crawford, H. Li, Y. Lee, X. Yuan, S. B. Kim, Y. S. Oh, W. J. Jang, J. Y. Lee, S. Han, J. Kim, X. Wang, Z. Xie, Y. Zhang, Y. Huang, J. A. Rogers, *ACS Nano* **2019**, *13*, 10972.
[74] X. Wang, X. Guo, J. Ye, N. Zheng, P. Kohli, D. Cho, Y. Zhang, Z. Xie, Q. Zhang, H. Luan, K. Nan, B. H. Kim, Y. Xu, X. Shan, W. Bai, R. Sun, Z. Wang, H. Jang, F. Zhang, Y. Ma, Z. Xu, X. Feng, T. Xie, Y. Huang, Y. Zhang, J. A. Rogers, *Adv. Mater.* **2019**, *31*, 1805615.
[75] K. Nan, H. Wang, X. Ning, K. A. Miller, C. Wei, Y. Liu, H. Li, Y. Xue, Z. Xie, H. Luan, Y. Zhang, Y. Huang, J. A. Rogers, P. V. Braun, *ACS Nano* **2019**, *13*, 449.

[76] M. Han, H. Wang, Y. Yang, C. Liang, W. Bai, Z. Yan, H. Li, Y. Xue, X. Wang, B. Akar, H. Zhao, H. Luan, J. Lim, I. Kandela, G. A. Ameer, Y. Zhang, Y. Huang, J. A. Rogers, *Nat. Electron.* **2019**, *2*, 26.
[77] G. P. T. Choi, L. H. Dudte, L. Mahadevan, *Nat. Mater.* **2019**, *18*, 999.
[78] L. H. Dudte, E. Vouga, T. Tachi, L. Mahadevan, *Nat. Mater.* **2016**, *15*, 583.
[79] H. Aharoni, Y. Xia, X. Zhang, R. D. Kamien, S. Yang, *Proc. Natl. Acad. Sci. USA* **2018**, *115*, 7206.
[80] Y. Xia, G. Cedillo-Servin, R. D. Kamien, S. Yang, *Adv. Mater.* **2016**, *28*, 9637.
[81] E. Siéfert, E. Reyssat, J. Bico, B. Roman, *Nat. Mater.* **2019**, *18*, 24.
[82] Y. Liu, Z. Yan, Q. Lin, X. L. Guo, M. D. Han, K. Nan, K. C. Hwang, Y. G. Huang, Y. H. Zhang, J. A. Rogers, *Adv. Funct. Mater.* **2016**, *26*, 2909.
[83] K. Pan, Y. Ni, L. He, R. Huang, *Int. J. Solids Struct.* **2014**, *51*, 3715.
[84] Z. C. Fan, K. C. Hwang, J. A. Rogers, Y. G. Huang, Y. H. Zhang, *J. Mech. Phys. Solids* **2018**, *111*, 215.
[85] M. Gazzola, L. H. Dudte, A. G. McCormick, L. Mahadevan, *R. Soc. Open Sci.* **2018**, *5*, 171628.
[86] M. K. Jawed, P. M. Reis, *Soft Matter* **2016**, *12*, 1898.
[87] M. A. Dias, B. Audoly, *J. Elasticity* **2015**, *119*, 49.
[88] C. Lestringant, B. Audoly, *J. Mech. Phys. Solids* **2017**, *103*, 40.
[89] C. Lestringant, C. Maurini, A. Lazarus, B. Audoly, *Phys. Rev. Lett.* **2017**, *118*, 165501.
[90] D. Zaccaria, D. Bigoni, G. Noselli, D. Misseroni, *Proc. R. Soc. A* **2011**, *467*, 1686.
[91] P. M. Reis, *J. Appl. Mech.* **2015**, *82*, 111001.
[92] M. Jawed, N. Khouri, F. Da, E. Grinspun, P. Reis, *Phys. Rev. Lett.* **2015**, *115*, 168101.
[93] Y. Chen, Y. Liu, Y. Yan, Y. Zhu, X. Chen, *J. Mech. Phys. Solids* **2016**, *95*, 25.
[94] A. M. Nasab, D. Wang, Z. Chen, W. Shan, *Extreme Mech. Lett.* **2017**, *15*, 51.
[95] G. Luo, H. Fu, X. Cheng, K. Bai, L. Shi, X. He, J. A. Rogers, Y. Huang, Y. Zhang, *J. Mech. Phys. Solids* **2019**, *129*, 261.
[96] Z. Yan, M. D. Han, Y. Y. Yang, K. W. Nan, H. W. Luan, Y. Y. Luo, Y. H. Zhang, Y. G. Huang, J. A. Rogers, *Extreme Mech. Lett.* **2017**, *11*, 96.
[97] H. R. Fu, K. W. Nan, P. Froeter, W. Huang, Y. Liu, Y. Q. Wang, J. T. Wang, Z. Yan, H. W. Luan, X. G. Guo, Y. J. Zhang, C. Q. Jiang, L. M. Li, A. C. Dunn, X. L. Li, Y. G. Huang, Y. H. Zhang, J. A. Rogers, *Small* **2017**, *13*, 1700151.
[98] Z. Xu, Z. Fan, Y. Zi, Y. Zhang, Y. Huang, *J. Appl. Mech.* **2020**, *87*, 031004.
[99] Z. Xu, Z. Fan, H. Fu, Y. Liu, Y. Zi, Y. Huang, Y. Zhang, *Phys. Rev. Appl.* **2019**, *11*, 054053.

